THE JOURNAL OF PHYSICAL CHEMISTRY A

Article

pubs.acs.org/JPCA

Solvent Effects on the Optical Spectra and Excited-State Decay of Triphenylamine-thiadiazole with Hybridized Local Excitation and Intramolecular Charge Transfer

Di Fan,[†,‡] Yuanping Yi,[‡] Zhendong Li,[ζ] Wenjian Liu,[ζ] Qian Peng,*[,‡] and Zhigang Shuai*[,†,ξ]

[†]College of Chemistry, Nanchang University, Nanchang 330031, People's Republic of China

[‡]Key Laboratory of Organic Solids, Beijing National Laboratory for Molecular Science (BNLMS), Institute of Chemistry, Chinese Academy of Sciences, Beijing 100190, People's Republic of China

[ξ]Key Laboratory of Organic OptoElectronics and Molecular Engineering, Department of Chemistry, Tsinghua University, Beijing 100084, People's Republic of China

[ζ]College of Chemistry and Molecular Engineering, Peking University, Beijing 100871, People's Republic of China

Supporting Information

ABSTRACT: The triphenylamine-thiadiazole molecule (TPA-NZP) is a newly popular, highly efficient OLED fluorescent emitter with exciton utilization efficiency exceeding the upper limit of spin statistics (25%). In this work, the optical spectra and the radiative and nonradiative decay rate constants have been investigated theoretically for TPA-NZP in hexane, ethyl ether, tetrahydrofuran, and dimethylformamide solvents, in comparison with the gas phase. We observed the evolutions of the excited states from the hybridized local and charge-transfer (HLCT) character to complete intramolecular charge transfer (CT) character with the increase of the solvent polarities. It is found that upon increasing the solvent polarity, the amount of red shift in the absorption peak is much less than that of emission, resulting in breakdown of the mirror symmetry. This is because that 0−0 transition energy is red-shifted but the vibrational relaxation increases with the solvent polarity, leading to subtraction in absorption while addition in emission. The radiative decay rate constant is calculated to be almost independent of polarity. The nonradiative decay rate increases by almost one order of magnitude from that in nonpolar hexane to the strongly polarized dimethylformamide, which is attributed to the dual effects of the red shift in the gap and enhancement of the vibrational relaxation by solvent polarity.

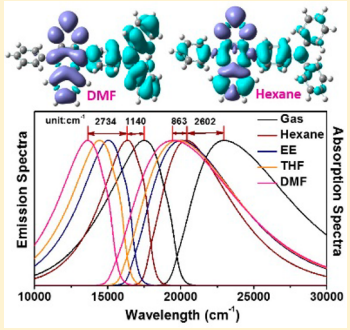

1. INTRODUCTION

Over the past two decades, the research on organic light-emitting diodes (OLEDs) still is attractive for its promising applications in flat-panel displays and solid-state lighting.[1−3] In the conventional fluorescent OLEDs, the charge carriers are injected electrically into the fluorphores to form three portions of triplet and one portion of singlet electron−hole pairs according to the spin statistics, and in general, 75% of the excitation energy can not be used due to spin symmetry. The organometallic phosphorescent emitters have been developed by using the strong spin−orbit couplings of transition metals (such as platinum and iridium) to harvest the triplet state, and the quantum efficiency has been boosted to nearly 100%.[4,5] The disadvantages of triplet emitters are efficiency drooping due to triplet−triplet annihilation and long lifetime. Recently, Adachi et al. have reported a new route to an efficient singlet emitter by using the thermally activated delayed fluorescence (TADF) phenomena with a class of donor−acceptor (D−A) fluorphores.[6,7] The key requirement of TADF molecules is very small singlet−triplet splitting energy. This needs a large separation in space between the highest occupied and lowest unoccupied molecular orbital wave function (HOMO and LUMO), which results in as small as possible overlap between them and the desired small singlet−triplet splitting energy. Undesirably, the radiative decay rate is reduced to as low as $\sim 10^6$ s^{-1} in due course. Therefore, it is necessary to come up with effective ways to restrain the nonradiative decay in order to obtain the high luminescence quantum efficiency from the light-emitting single state.

Alternately, Ma et al. have put forward a novel kind of fluorphore with the lowest excited state consisting of hybridized local and charge-transfer (HLCT) and OLED devices based on them beating the spin statistical limit of 25% because of the bottleneck effect preventing the internal conversion from T_2 to T_1.[8,9] Through both the fluorescent solvatochromic experiment and quantum chemical calculation for the molecules in the gas phase, it is shown that the hybridization of local excitation (LE) and charge transfer (CT) for the lowest excited state is imperative. The LE with the electronic transitions in the same moiety exhibits a large electric transition dipole moment for the

Special Issue: Jacopo Tomasi Festschrift

Received: October 1, 2014
Revised: November 10, 2014
Published: November 17, 2014

dx.doi.org/10.1021/jp5099409 | J. Phys. Chem. A 2015, 119, 5233−5240

lowest excited state, while the CT character results in a small exchange energy at higher excited states, facilitating the interconversion between triplet and singlet manifolds. In this work, through computational study, we elucidate the photophysical properties such as absorption and emission spectra and radiative and nonradiative decay rates as a function of solvent polarity.

Understanding solvation effects on the photophyscial behaviors has been the focus of research in both experimental and theoretical studies.[10−13] Here, we chose the typical HLCT deep red *N*,*N*-diphenyl-4-(9-phenylnaphtho-[2,3-*c*][1,2,5]-thiadiazol-4-yl)aniline (TPA-NZP) molecule shown in Chart 1 to calculate quantitatively its optical spectra and radiative and nonradiative decay rate constants in the gas phase and hexane, ethyl ether (EE), tetrahydrofuran (THF), and dimethylformamide (DMF) solvents. The evolution processes of the excited states have been examined when going from nonpolar to strong polar solvents, and the effects of solvent polarities on the spectra and excited-state decay rates have been analyzed quantitatively in detail.

Chart 1. Chemical Structure of TPA-NZP

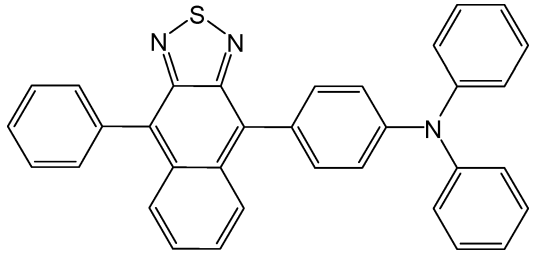

2. METHODOLOGY

2.1. Optical Spectra. On the basis of the Fermi's golden rule (FGR) and the Franck−Condon principle, the absorption spectrum $\sigma_{ab}(\omega,T)$ and the emission spectrum $\sigma_{em}(\omega,T)$ are written as[14]

$$\sigma_{ab}(\omega, T) = \frac{4\pi^2\omega}{3\hbar c}|\boldsymbol{\mu}_{fi}|^2 \sum_{u,\nu} P_{i\nu}|\langle\Theta_{fu}|\Theta_{i\nu}\rangle|^2\delta(\omega - \omega_{fu,i\nu}) \tag{1}$$

$$\sigma_{em}(\omega, T) = \frac{4\omega^3}{3\hbar c^3}|\boldsymbol{\mu}_{fi}|^2 \sum_{u,\nu} P_{i\nu}|\langle\Theta_{fu}|\Theta_{i\nu}\rangle|^2\delta(\omega_{i\nu,fu} - \omega) \tag{2}$$

Here, $\hbar$ is the Planck constant, c means the speed of light, $P_{i\nu}$ represents the Boltzmann distribution function for the initial-state vibronic manifold at the finite temperature, Θ denotes the nuclear vibrational wave function, ν and u are the vibrational quantum numbers of the initial and final state, respectively, and $\boldsymbol{\mu}_{fi}$ is the electric transition dipole moment between the two electronic states $|\Phi_i\rangle$ and $|\Phi_f\rangle$, independent of the nuclear coordinate under the Franck−Condon approximation.

Using the thermal vibration correlation function (TVCF) method, eqs 1 and 2 can be recast into time-dependent forms

$$\sigma_{ab}^{FC}(\omega, T) = \frac{2\pi\omega}{3\hbar c}|\boldsymbol{\mu}_{fi}|^2 \int_{-\infty}^{\infty} e^{i(\omega-\omega_{fi})t} Z_i^{-1}\rho_{ab,0}^{FC}(t, T)\, dt \tag{3}$$

$$\sigma_{em}^{FC}(\omega, T) = \frac{2\omega^3}{3\pi\hbar c^3}|\boldsymbol{\mu}_{fi}|^2 \int_{-\infty}^{\infty} e^{-i(\omega-\omega_{if})t} Z_i^{-1}\rho_{em,0}^{FC}(t, T)\, dt \tag{4}$$

in which Z_i is the partition function; the TVCFs $\rho_{ab,0}^{FC}(t,T)$ and $\rho_{em,0}^{FC}(t,T)$ have the same form $\mathrm{Tr}[e^{-i\tau_f}\hat{H}_f e^{-i\tau_i}\hat{H}_i]$ and can be solved analytically by multidimensional Gaussian integrations.[15] Here, $\tau_i = -i\beta - (t/\hbar)$, $\tau_f = t/\hbar$, $\beta = (k_B T)^{-1}$, and $\hat{H}_f$ ($\hat{H}_i$) is the harmonic oscillator Hamiltonian of the final (initial) electronic state.

2.2. Radiative and Nonradiative Decay Rate Constants. The radiative decay rate constant is the integration over the emission spectrum

$$k_r(T) = \int \sigma_{em}(\omega, T)\, d\omega \tag{5}$$

According to the FGR and first-order perturbation theory, the nonradiative decay rate constant can be expressed as

$$k_{NR} = \frac{2\pi}{\hbar}\sum_{u,\nu} P_{i\nu}|\hat{H}'_{fu,i\nu}|^2\delta(E_{i\nu} - E_{fu}) \tag{6}$$

where H' denotes the interaction between two different Born−Oppenheimer states, consisting of two contributions as follows

$$\hat{H}'\Psi_{i\nu} = \hat{H}^{BO}\Phi_i(\mathbf{r};\mathbf{Q})\Theta_\nu(\mathbf{Q}) + \hat{H}^{SO}\Phi_i(\mathbf{r};\mathbf{Q})\Theta_\nu(\mathbf{Q}) \tag{7}$$

Here, $\hat{H}^{BO}$ is the nonadiabatic coupling, and $\hat{H}^{SO}$ is spin−orbit coupling. When the small term $\partial^2\Phi_i/\partial Q_{fl}^2$ is neglected, the first term reads

$$\begin{aligned}&\langle\Phi_f\Theta_{fu}|\hat{H}^{BO}|\Phi_i\Theta_{i\nu}\rangle \\ &= -\hbar^2\sum_l \left\langle \Phi_f\Theta_{fu}\middle|\frac{\partial\Phi_i}{\partial Q_{fl}}\frac{\partial\Theta_{i\nu}}{\partial Q_{fl}}\right\rangle \\ &= \sum_l \langle\Phi_f\Theta_{fu}|(\hat{P}_{fl}\Phi_i)(\hat{P}_{fl}\Theta_{i\nu})\rangle\end{aligned} \tag{8}$$

where l is the index of the normal mode and $\hat{P}_{fl}$ is the normal momentum operator of the lth normal mode in the final electronic state.

The internal conversion rate constant between two electronic states with same spin manifold can be written as[16]

$$k_{IC} = \frac{2\pi}{\hbar}\sum_{kl} R_{kl}Z_i^{-1}\sum_{\nu,u} e^{-\beta E_{i\nu}}\langle\Theta_{fu}|\hat{P}_{fk}|\Theta_{i\nu}\rangle\langle\Theta_{i\nu}|\hat{P}_{fl}|\Theta_{fu}\rangle\delta(E_{i\nu} - E_{fu}) \tag{9}$$

where $R_{kl} = \langle\Phi_f|\hat{P}_{fk}|\Phi_i\rangle\langle\Phi_i|\hat{P}_{fl}|\Phi_f\rangle$ is the nonadiabatic electronic coupling. Applying the Fourier transform of the delta function, eq 9 is recast as

$$k_{IC} = \sum_{kl}\frac{1}{\hbar^2}R_{kl}\int_{-\infty}^{\infty} dt\ [e^{i\omega_{if}t}Z_i^{-1}\rho_{IC}(t, T)] \tag{10}$$

where $\rho_{IC}(t,T)$ is the TVCF of $\mathrm{Tr}(\hat{P}_{fk}e^{-i\tau_f}\hat{H}_f\hat{P}_{fl}e^{-i\tau_i}\hat{H}_i)$.

Similarly, the nonradiative intersystem crossing rate constant between two electronic states with different spin states can be described as

$$k_{ISC} = \frac{1}{\hbar^2}\langle\Phi_f|\hat{H}^{SO}|\Phi_i\rangle\int_{-\infty}^{\infty} dt\ [e^{i\omega_{if}t}Z_i^{-1}\rho_{ISC}(t, T)] \tag{11}$$

Here, the TVCF form is $\rho_{ISC}(t,T) = \mathrm{Tr}[e^{-i\tau_f}\hat{H}_f e^{-i\tau_i}\hat{H}_i]$, namely, the same Franck−Condon factor as that in eqs 3 and 4. These TVCFs have been solved analytically by multidimensional

dx.doi.org/10.1021/jp5099409 | J. Phys. Chem. A 2015, 119, 5233−5240

Gaussian integrations. Both the methodology and application of this formalism can be found in our previous work.[17−19]

2.3. Computational Details. The geometry optimizations and frequency calculations were performed for the ground (S_0) and lowest triplet (T_1) states by using density functional theory (DFT) and for the lowest singlet (S_1) state by employing time-dependent DFT (TD-DFT) with the B3LYP hybrid functional and 6-31G(d,p) basis set. The long-range interactions were considered through single-point energy calculation with the CAM-B3LYP functional. The solvent environments were mimicked by using the polarizable continuum model (PCM),[20,21] in which the equilibrium solvation method was applied for the geometry optimization and the nonequilibrium solvation one was adopted for the single-point calculation at the equilibrium geometry.[22] The state-specific method was chosen to compute the excited-state property.[23,24] These quantities are calculated with the Gaussian 09 package.[25]

On the basis of the electronic structure information, the spectra and the radiative, internal conversion, and intersystem crossing rate constants were evaluated by using the TVCF theory in the MOMAP program developed in our group.[16,17,26] Herein, the difference between two electronic state potential energy surfaces (PESs) was considered by using $\underline{Q}_e = \boldsymbol{S}\underline{Q}_g + \underline{D}_e$. Here, $\boldsymbol{S}$ is the Duschinsky rotation matrix (DRM) and is obtained by $\boldsymbol{S} = \mathbf{L}_i^T\mathbf{L}_f$ ($\mathbf{L}_{i(f)}$ is the mass-weighted normal modes of the initial (final) state). The vector $\mathbf{D}$ is the displacement between the minima of the ground- and excited-state geometries of $\mathbf{D}_{i(f)} = \mathbf{L}_{i(f)}^T\Delta x$ (Δx is the displacement in Cartesian coordinates). The nonadiabatic electronic coupling term was treated as the force acting on the atomic nuclei through the transition electric field under the frame of the first-order perturbation theory,[27] and the transition electric field was evaluated by using TDDFT in the Gaussian 09 package. The spin−orbit coupling matrix elements were calculated at the TDDFT level[28] with the first-order DKH-like spin−orbit operator derived[29] from the exact two-component Hamiltonian.[30] This set of calculations was performed with the BDF program package.[31]

3. RESULTS AND DISCUSSION

3.1. Molecular Geometric Structures. First, the geometries were fully optimized at the S_0, S_1, and T_1 states at the B3LYP/6-31G(d,p) level for TPA-NZP in the gas phase and hexane, EE, THF, and DMF solvents. The PCM was employed for taking the solvent effect into account. The equilibrium solvation was applied for the geometry optimization because in this situation, the solvent had time to fully respond to the changes the solute in both ways, polarizing its electron distribution and making its nuclei reoriented. The frequencies at the $\mathbf{S_0}$ and $\mathbf{S_1}$ equilibrium geometries were computed at the same level, and there were no imaginary frequencies. The atomic labels, the interesting dihedral angles, and the index of the phenyl ring are given in Figure 1. The optimized structural parameters at the $\mathbf{S_0}$ and $\mathbf{S_1}$ equilibrium geometries of TPA-NZP in different solvents are listed in Table 1 and Table S1 in the Supporting Information (SI), as well as their modifications Δ_{S1-S0} between two electronic states. We found that the S_0 geometries hardly vary in the gas phase and the solvents with various polarities, while the S_1 geometries show large modifications when going from the gas phase to solvent phase. For example, θ2, θ3, and θ4 are all increased by ∼7−10° in the solvents when compared with those in the gas phase. Comparing the S_0 and S_1 geometries, the large geometric

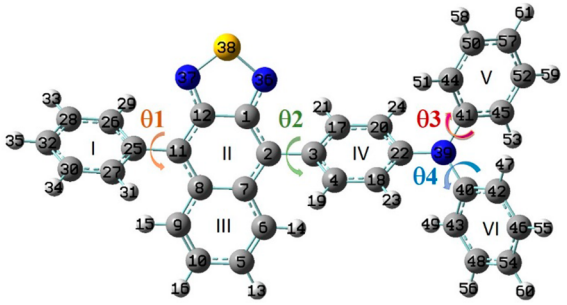

Figure 1. Atomic labels, the interesting dihedral angles, and the index of the phenyl ring of TPA-NZP: θ1 = D(27−25−11−8), θ2 = D(1−2−3−4), θ3 = D(22−39−41−44), and θ4 = D(22−39−40−43).

relaxations mainly appear in the dihedral angels θ1, θ3, and θ4 in the gas phase, while they dominantly contribute to θ1 and θ2 in the solvent phase. The difference is easily understood because TPA-NZP is very flexible with rotatable phenyl rings. The phenyl rings in the periphery (e.g., θ1, θ3, and θ4) could rotate more freely in the gas phase and be restricted to some extent in the solvent. However, the θ2 links the electron-withdrawing naphthothiadiazole (NZ) moiety and the electron-donating TPA moiety, which inevitably is affected by the polarity of the solvent. The bond lengths have slight modifications on the N−S and C−C bonds of the NZ moiety in the gas and solvent phases.

3.2. Excited-State Properties. The standard linear response solvation method can give a reasonable description of the solvation of the excited state when identifying the ordering of excited states. However, the excitation energy obtained is not quite as good as that from a state-specific solvation calculation in which the solvent reaction field is made self-consistent with the solute electrostatic potential. The state-specific method has been widely used to simulate the optical properties of organic molecules in solvent.[32−35] However, some authors found that the state-specific method sometimes generated unphysical values for the strong CT molecules.[36] We first compared the adiabatic energies calculated by using the standard linear response and state-specific PCM methods coupled with the long-range separated functional CAM-B3LYP in Table S2 in the SI. The results indicate that the adiabatic energies obtained by the latter are decreasing as the polarities are increasing, which are in good agreement with the spectroscopic red shifts observed experimentally. Therefore, we chose the state-specific PCM to provide the excited-state structure information for the following analysis of the transition properties and calculations of the spectra and rates of TPA-NZP in the solvents. Figures 2 and 3 show the molecular orbital energy levels and the transition proportions and the corresponding electron density contours of the molecular orbitals at the S_0 geometries, respectively. The highest occupied molecular orbitals (HOMOs) are almost identical both in energy and in electron density distribution for TPA-NZP in the gas phase and in nonpolar hexane. However, with the increase of the solvent polarity, the HOMOs are gradually going up in energy due to the electron density of the HOMO being more and more localized on the donor subunit TPA. The lowest unoccupied molecular orbitals (LUMOs) are going down in energy with increasing solvent polarity, while the electron densities are always localized on the acceptor subunit NZ regardless of the solvent polarity. We checked independently the solvent effect on the NZ molecule. The solvation only

dx.doi.org/10.1021/jp5099409 | J. Phys. Chem. A 2015, 119, 5233−5240

Table 1. Selected Structural Parameters of TPA-NZP in Different Solvents at the S_0 (S_1) Optimization Geometries at the B3LYP/6-31G(d,p) Level in Degrees

	θ1			θ2			θ3			θ4		
	S_0	S_1	Δ_{S1-S0}	S_0	S_1	Δ_{S1-S0}	S_0	S_1	Δ_{S1-S0}	S_0	S_1	Δ_{S1-S0}
gas	57.6	51.4	−6.2	124.6	124.2	−0.4	42.4	34.0	−8.4	44.3	35.1	−9.2
hexane	58.5	49.4	−9.1	123.7	131.1	7.4	42.8	40.7	−2.1	44.8	41.3	−3.5
EE	59.5	49.7	−9.8	122.9	132.8	9.9	43.1	43.0	−0.1	45.2	43.8	−1.4
THF	60.0	50.1	−9.9	122.5	133.3	10.8	43.3	43.9	0.6	45.4	44.5	−0.9
DMF	60.4	50.9	−9.5	122.1	133.8	11.7	43.7	44.9	1.2	45.6	45.3	−0.3

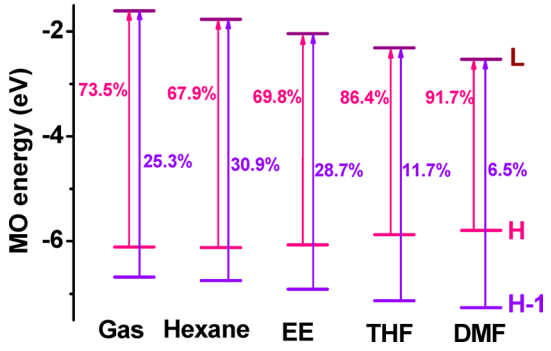

Figure 2. Molecular orbital energy levels and the transition properties at S_0 geoemtries of TPA-NZP in the gas phase and various solvents.

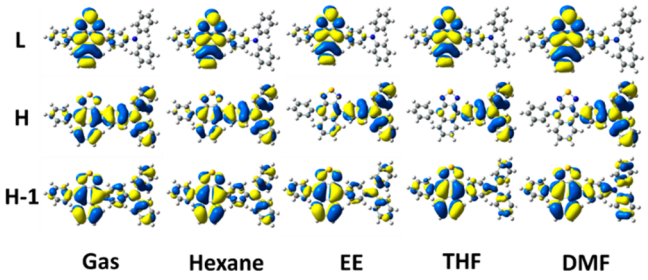

Figure 3. Electron density contours of molecular orbitals LUMO (L, top), HOMO (H, middle), and HOMO−1 (H−1, bottom) at S_0 geoemtries of TPA-NZP in the gas phase and various solvents.

stabilizes the LUMO in energy and has hardly no impact on the electron density distribution. Similarly, the energy of HOMO−1 is decreased by the polarity, while the electron density distribution hardly changes.

In all cases, the main contributions to the emissive S_1 state mainly come from the transitions of the HOMO → LUMO and the HOMO−1 → LUMO. Their relative proportions, however, undergo significant changes when going from the gas phase to nonpolar and more polar solvents. The component percentage of HOMO → LUMO progressively rises from 67.9 to 91.7%; correspondingly, HOMO−1 → LUMO steadily falls from 30.9 to 6.5% upon changing solvents from nonpolar hexane to strong polar DMF. The transition component proportion in the gas phase is similar to that in the solvent with moderate polarity. Therefore, the partial intramolecular CT characters were observed in the gas phase and nonpolar and moderately polar solvents, while the entire intramolecular CT was seen in strong polar solvent. Consequently, the energy gaps between two electronic states was reduced as the solvent polarities strengthened. In addition, Figures S1 and S2 of the SI give the molecular orbital energy levels and the transitions and the corresponding electron density contours of the molecular orbitals at the S_1 geometries, respectively. The HOMOs are almost independent of the polarity. The LUMOs are reduced in energy by the polarity. The S_1 state is dominated by the transition from HOMO to LUMO of ∼82%, regardless of the polarity. These strongly indicate that compared to the excited-state electronic structural properties at the S_0 geometry, those at the S_1 geometry are less sensitive to the polarity.

In order to directly characterize the localized excitation and CT behaviors, we calculated the charge density differences between the S_1 and S_0 states at the S_0 geometries of TPA-NZP in different solvents by using $\Delta\rho(r) = \rho^{ele}(r) - \rho^{hole}(r)$[37] and plotted them in Figure 4. We can see that (i) the electron

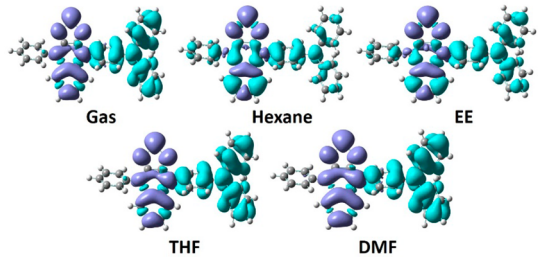

Figure 4. Charge density differences between the S_1 and S_0 states of TPA-NZP at S_0 geometies of TPA-NZP in the gas phase and various solvents.

always localizes on the acceptor NZ moiety regardless of polarity, (ii) the hole delocalizes over the whole molecule, including acceptor NZ and donor TPA moieties in nonpolar hexane, (iii) with the solvent polarity increasing, the hole gradually transfers to the donor TPA moiety, and (iv) in the strongest polar DMF, the hole almost completely concentrates on the TPA moiety. Thus, the hole and electron on a molecule are entirely separated, and such an excited state becomes an intramolecular CT excited state. If the hole and the electron totally distribute on the same moiety, the excited state is a LE one. Then, between the two conditions, the excited state belongs to the HLCT state, just like that in hexane. These confirm that the excited state evolves from HLCT to CT states with the increase of the solvent polarities. The charge density differences between two electronic states at the S_1 geometries are plotted in Figure S3 of the SI. The charge differences are insensitive to the polarity, which is perfectly consistent with the corresponding excited-state structures discussed above.

3.3. Optical Spectra. On the basis of the electronic structure information on TPA-NZP in different solvents, the absorption and emission spectra at 300 K were calculated by considering the displaced, distorted, and Duschinsky rotation effects between S_1 and S_0 and were presented in Figure 5 as well as the full width at half-maximum (fwhm) of the spectra. We found that (i) in the gas phase and solvents, the absorption spectra are structureless while the emission spectra have one

dx.doi.org/10.1021/jp5099409 | J. Phys. Chem. A 2015, 119, 5233−5240

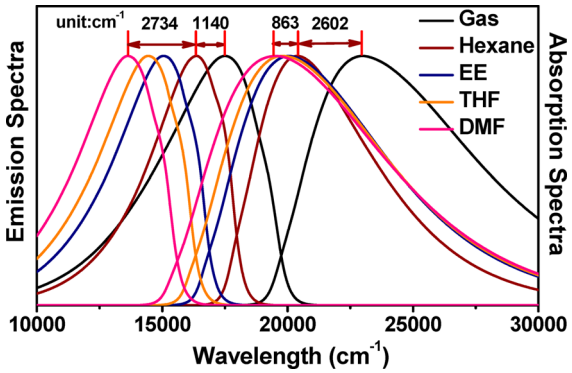

Figure 5. Absorption and emission spectra at 300 K of TPA-NZP in the gas phase and various solvents. The fwhms of absorption and emission spectra are 7765 and 4829 cm^{-1} in the gas phase, 5529 and 3577 cm^{-1} in hexane, 7015 and 3885 cm^{-1} in EE, 7487 and 3928 cm^{-1} in THF, and 8050 and 3952 cm^{-1} in DMF, respectively.

shoulder, (ii) compared to the spectra in the gas phase, the absorption spectrum is red-shifted sharply by 2602 cm^{-1} and the emission one is red-shifted by 1140 cm^{-1} in nonpolar hexane, (iii) relative to the spectra in hexane, the absorption spectrum exhibits a little red shift while the emission spectrum demonstrates a large bathochromic shift with increasing solvent polarity, and (iv) the values of Stokes shifts (κ), that is, the difference between the absorption and emission maxima, increase with the increasing solvent polarity. These are 4020, 4991, 5349, and 5891 cm^{-1} for TPA-NZP in hexane, EE, THF, and DMF, respectively, and the κ in the gas phase is 5482 cm^{-1}, close to that in moderate polarity THF solvent. (v) Finally, the fwhm is dependent on the polarity. It reaches 8050 cm^{-1} in DMF, namely, 2521 cm^{-1} larger than that in nonpolar hexane. Moreover, the widths of the absorption spectra are larger than those of the emission spectra. In addition, in order to visually compare to the experimental spectra, we plotted the calculated spectra versus the wavelengths in Figure S4 and made corresponding discussions in SI. The calculated results, including shapes of the spectra and Stokes shifts, and the solvatochromic shifts, are in good agreement with the experimental counterparts.[8]

In order to gain insight of the spectral behaviors, we simply sketched the light-absorbing and -emitting processes between the S_0 and S_1 states based on their identical PESs (see Figure 6). Here, E_{abs}^{peak} (E_{em}^{peak}) represents the maximum peak position of the absorption (emission) spectrum; ΔE_{ad} is the adiabatic excitation energy (E_{0-0}) between the two electronic states. $\lambda_{gs(es)}$ is the reorganization energy from the nonequilibrium geometry relaxing to the equilibrium one at the S_0 PES (S_1 PES), and the λ_l of the lth normal mode can be obtained by the product of the Huang−Rhys factor and the vibrational energy

$$\lambda = \sum_l \lambda_l = \sum_l S_l \hbar\omega_l \tag{12}$$

where

$$S_l = \frac{\omega_l}{2\hbar}\Delta D^2 \tag{13}$$

According to the Franck−Condon principle, the maximum peak in the optical spectra occurs at the vertical transition; see Figure 6

$$E_{abs}^{peak} = E_{0-0} + \lambda_{es} \qquad E_{em}^{peak} = E_{0-0} - \lambda_{gs} \tag{14}$$

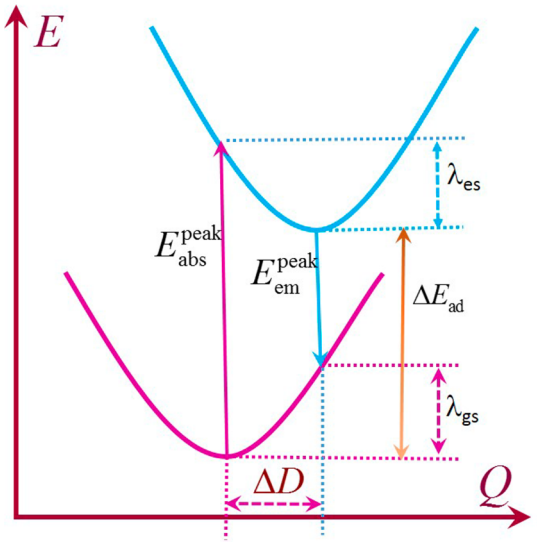

Figure 6. Sketch of the PESs at the S_0 and S_1 states.

The solvatochromic shifts are then given by

$$\delta_{abs}^{peak} = \delta(E_{0-0}) + \delta(\lambda_{es}) \qquad \delta_{em}^{peak} = \delta(E_{0-0}) - \delta(\lambda_{gs}) \tag{15}$$

and the Stokes shift κ corresponds to the total reorganization energy

$$\kappa = \lambda_{gs} + \lambda_{es} \tag{16}$$

Table 2 shows the calculated E_{0-0} and $\lambda_{gs(es)}$ of TPA-NZP in the gas phase and solvents at the S_0 PES or S_1 PES, as well as the corresponding modifications relative to the values in the gas phase. From Table 2, $\delta(E_{0-0})$ is always negative (red shift). Owing to the restriction of the phenyl rings (θ3 and θ4) in the solvent phase, the reorganization energy becomes smaller in nonpolar hexane, $\delta(\lambda_{es}) < 0$ and $\delta(\lambda_{gs}) < 0$, which leads to $\delta_{abs}^{peak} > \delta_{em}^{peak}$, just like the observations in Figure 5. The polarity induces the large vibrational relaxation and makes the reorganization energy in the weak polar EE larger than that in the gas phase, $\delta(\lambda_{gs}) > 0$ and $\delta(\lambda_{es}) > 0$. Moreover, the λ_{es} and λ_{gs} both rise as the solvent polarity increases. As a result, a considerable difference in solvatochromic shifts for the absorption and emission spectra appears when going from nonpolar to more polar solvents. Accordingly, it is evident that the increase of the Stokes shift and the fwhm both are caused by the increase of the reorganization energies when the solvent polarity increases.

Next, we calculated the absorption and emission spectra in different solvents at 0 K by using the displaced−distorted harmonic model,[38] which is presented in Figure 7 along with the assignments of some typical peaks. It is observed that (i) the 0−0 transitions are red-shifted with solvent polarity, (ii) the maximum peak does not appear at the 0−0 transition position because the largest Huang−Rhys factor is larger than 1.0 in all of the solvents (Table S3 of SI), and (iii) the spectra are quite smooth even at 0 K because the contributions of low-frequency modes and their combinations dominate vibrational relaxation processes.

3.4. Radiative and Nonradiative Decay Rate Constants. Starting from the S_1 state, the excited-state decay processes include the radiative decay from S_1 to S_0, the nonradiative internal conversion from S_1 to S_0, and the

dx.doi.org/10.1021/jp5099409 | J. Phys. Chem. A 2015, 119, 5233−5240

Table 2. Calculated E_{0-0} and $\lambda_{gs(es)}$ for TPA-NZP in the Gas Phase and Solvents at the S_0 PES or S_1 PES

	E_{0-0} /eV	$\delta(E_{0-0})$ /cm^{-1}	λ_{gs} /cm^{-1}	$\delta(\lambda_{gs})$ /cm^{-1}	λ_{es} /cm^{-1}	$\delta(\lambda_{es})$ /cm^{-1}
gas	2.479	0.0	1471.7	0.0	1790.2	0.0
hexane	2.239	−1935.8	1272.3	−199.4	1518.5	−271.7
EE	2.086	−3169.9	1502.6	30.9	1824.2	34.0
THF	2.014	−3750.7	1568.6	96.9	1944.9	154.7
DMF	1.919	−4517.0	1645.2	173.5	2109.6	319.4

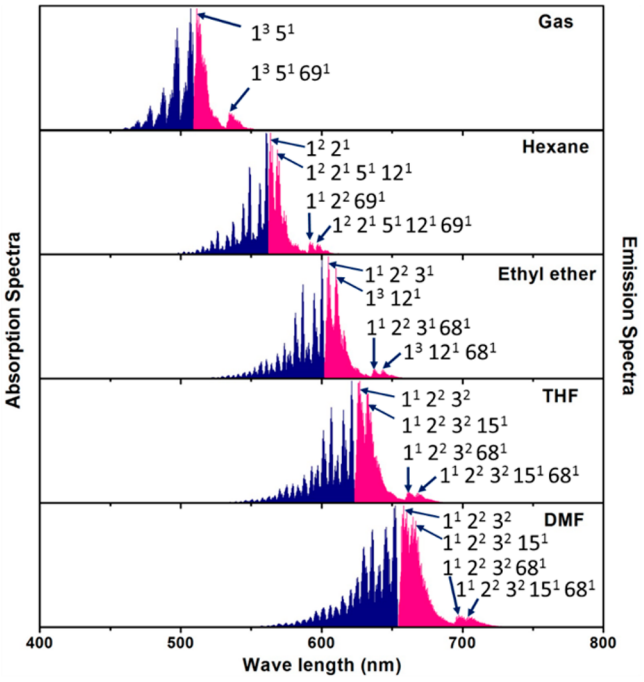

Figure 7. Absorption and emission spectra at 0 K of TPA-NZP in different solvents, as well as the assignments of the selected peaks with n^m, where n is the normal mode index and m the vibrational quantum number.

nonradiative intersystem crossing from S_1 to T_1. By using the TVCF method, the radiative and nonradiative decay rate constants were calculated, respectively. It is similar to the spectrum calculations; the difference between the S_1 and S_0 states was considered through displacement, distortion, and Duschinsky rotation effects. The intersystem crossing rate constant is calculated to be 0.1−7 × 10^5 S^{-1}, 2 orders of magnitude lower than the radiative decay rates owing to very small spin−orbit coupling matrix elements between S_0 and T_1 (see Table S4 in the SI). Therefore, we mainly focus on the radiative and internal conversion rate constants in the following, and the relevant values are shown in Table 3.

From Table 3, it can be seen that the radiative rate constants are almost independent of the solvent polarity. From the simple Einstein spontaneous emission relationship formula $k_r = f\Delta E^2/1.449$, we can know that the oscillator strength and the excitation energy are two very important factors. Here, the oscillator strengths are insensitive to the polarity, which corresponds to the insensitivity of the excited-state property to the polarity at the S_1 geometry.

In contrast, the nonradiative internal conversion rate constants are much more sensitive to the polarity and increased by almost 1 order of magnitude from hexane to DMF. Such an increment is due to two reasons that (i) the vibrational relaxation energy increases with solvent polarity (Table 2) and (ii) the energy gap is red-shifted. Thus, the k_{IC} of TPA-NZP would increase when going from non-polar to more polar solvents. Figure 8 plots the scaled nonadiabatic coupling matrix

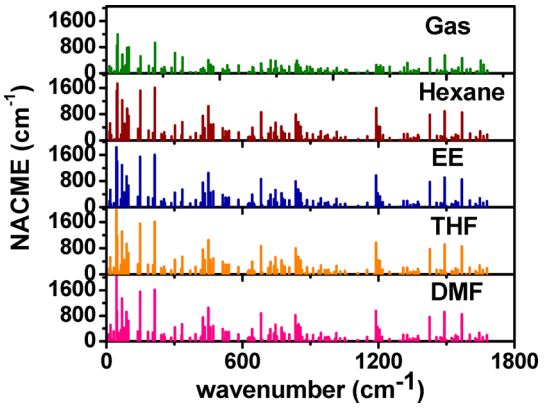

Figure 8. Scaled NACME for TPA-NZP versus the wavenumber of the normal mode at the ground-state PES. Scaled NACME = $(\hbar/\omega_l)^{1/2}\langle\Phi_f|(\partial V/\partial Q_l)|\Phi_i\rangle$.

elements (NACMEs) versus the wavenumber of normal vibrational modes. It can be seen that many vibrational modes contribute to the nonadiabatic coupling (prefactor in eq 9). Namely, it is impossible to define a so-called promoting mode. This fully justifies our development of a promoting-free formalism.[16,39] The displacement vectors of the important normal modes with a large scaled NACME are given in Figure S5 of the SI. The normal modes mainly belong to the rotations of phenyl rings at different positions. For example, the normal mode with the largest scaled NACME is assigned as the ratio of motions of two phenyl rings P−I and P−IV around the molecular central long axis. The similar scaled NACMEs in the solvents do not cause the difference of the IC rate constants.

Table 3. Oscillator Strengths f and Radiative and Nonradiative Decay Rate Constants of TPA-NZP in the Gas Phase and Various Solvents

	gas	hexane	EE	THF	DMF
f	0.2759	0.3053	0.3064	0.3053	0.3060
k_r/s^{-1}	3.25 × 10^7	3.80 × 10^7	2.73 × 10^7	2.38 × 10^7	2.02 × 10^7
k_{IC}/s^{-1}	6.33 × 10^{10}	3.41 × 10^{10}	1.28 × 10^{10}	1.59 × 10^{11}	1.83 × 10^{11}
k_{ISC}/s^{-1}	5.23 × 10^5	6.76 × 10^5	2.57 × 10^5	2.19 × 10^5	1.01 × 10^4

dx.doi.org/10.1021/jp5099409 | J. Phys. Chem. A 2015, 119, 5233−5240

However, the scaled NACMEs in the gas phase are obviously smaller than those in all solvents, which would lessen the IC rate constant in the gas phase. Figure 9 shows the

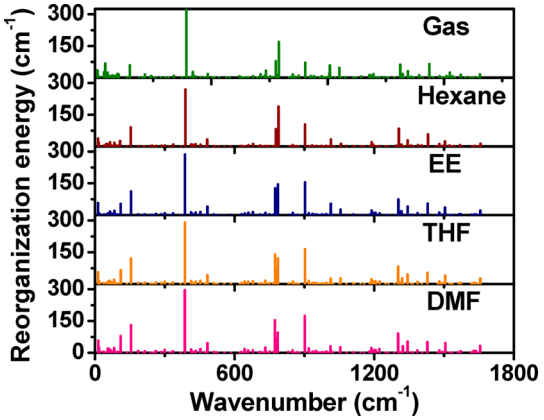

Figure 9. Reorganization energy of TPA-NZP versus the wavenumber of the normal mode at the ground-state PES.

reorganization energies (vibration relaxation) of each normal mode. There are few normal modes with significant reorganization energies for the TPA-NZP in the solvents. These contributions always come from the same normal modes both in the gas phase and in various solvents. The reorganization energies increase with the increase of solvent polarities, responsible for the increase of the IC rate. In addition, the combination of the restriction and polarization in solvent makes the IC rate constant in moderate solvent closer to that in the gas phase.

4. CONCLUSION

On the basis of the PCM model coupled to the quantum chemistry calculations, we have investigated theoretically the photophysical properties of TPA-NZP in solvents with various polarities by using the TVCF method. We found that the ground-state geometries are almost polarity-independent, while the lowest singlet excited-state geometries are solvent-dependent. Taking the distribution of the charge density difference between S_1 and S_0 states as an example, in nonpolar hexane, the hole spreads over the whole molecule; with the solvent polarity increasing, the hole continually transfers from the NZ moiety (behaving as an electron acceptor) to TPA (behaving as an electron donor); in strong polar DMF, the hole and electron are entirely separated, with the hole on the TPA moiety and the electron on the NZ moiety. The charge density difference at the S_1 geometries is insensitive to the polarity. Therefore, we clearly observed the evolutions of the excited states from the HLCT entirely to CT characters with the increase of the solvent polarities at the S_0 geometries.

The polarity induces a red shift in the adiabatic transition energy E_{0-0} but increases the vibrational relaxation. These rationally explain the calculated and experimental phenomena; the absorption spectra have a slight red shift, while the emission spectra exhibit a large red shift when increasing the solvent polarity, and the Stokes shifts become larger in more polar solvent.

The radiative decay rate constant of TPA-NZP is about $\sim 10^7$ s^{-1}, which is smaller than that of strong fluorescent organic molecules of $\sim 10^8$ s^{-1} but larger than that of the typical CT molecules (TADF molecule) of $\sim 10^6$ s^{-1}. This strongly suggests the lowest singlet excited state of TPA-NZP has hybrid localized excitation and CT character. The radiative decay rate constants are found to be insensitive to the solvent polarity. The internal conversion rate constant increases sharply by 1 order of magnitude when going from nonpolar hexane to strong polar DMF. This stems from the dual effects of the decrease in transition energy and the increase in vibrational relaxation. The major limitation of the present study is the assumption of a harmonic oscillator. Even though the origin displacement and parabola distortion are considered, anharmonicity and nonperturbativity are not considered, which deserves further investigation.[40] The MOMAP program used in this work can be obtained free of charge from Ref. 41.

■ ASSOCIATED CONTENT

Supporting Information

Supplementary structure parameters of TPA-NZP in different solvents at the S_0 (S_1) optimization geometries; molecular orbital energy levels, the transitions, and the corresponding electron density contours of molecular orbitals at S_1 geometries; charge density differences between the S_1 and S_0 at S_1 geometies; absorption and emission spectra at 300 K of TPA-NZP in the gas phase and various solvents; the displacement vectors of the normal modes with large NACME and the spin−orbit coupling matrix elements between S_1 and T_1. This material is available free of charge via the Internet at http://pubs.acs.org.

■ AUTHOR INFORMATION

Corresponding Authors

*E-mail: qpeng@iccas.ac.cn (Q.P.)
*E-mail: zgshuai@tsinghua.edu.cn (Z.S.).

Notes

The authors declare no competing financial interest.

■ ACKNOWLEDGMENTS

The authors are acknowledging here Prof. Bing Yang for valuable experimental discussions. The work is supported by the National Natural Science Foundation of China (Grants 21290191, 91233105, and 21473214), the Ministry of Science and Technology of China through the 973 program (Grants 2013CB834703, 2015CB65502, and 2013CB933503), and the Strategic Priority Research Program of the Chinese Academy of Sciences (Grant XDB12020200).

■ REFERENCES

(1) Tang, C. W.; VanSlyke, S. A. Organic Electroluminescent Diodes. *Appl. Phys. Lett.* **1987**, *51*, 913−915.
(2) Burroughes, J. H.; Bradley, D. D. C.; Brown, A. R.; Marks, R. N.; Mackay, K.; Friend, R. H.; Burns, P. L.; Holmes, A. B. Light-Emitting Diodes Based on Conjugated Polymers. *Nature* **1990**, *347*, 539−541.
(3) Han, T.-H.; Lee, Y.; Choi, M.-R.; Woo, S.-H.; Bae, S.-H.; Hong, B. H.; Ahn, J.-H.; Lee, T.-W. Extremely Efficient Flexible Organic Light-Emitting Diodes with Modified Graphene Anode. *Nat. Photonics* **2012**, *6*, 105−110.
(4) Baldo, M. A.; O'Brien, D. F.; You, Y.; Shoustikov, A.; Sibley, S.; Thompson, M. E.; Forrest, S. R. Highly Efficient Phosphorescent Emission from Organic Electroluminescent Devices. *Nature* **1998**, *395*, 151−154.
(5) Ma, Y. G.; Zhang, H. Y.; Shen, J. C.; Che, C. M. Electroluminescence from Triplet Metal−Ligand Charge-Transfer Excited State of Transition Metal Complexes. *Synth. Met.* **1998**, *94*, 245−248.

(6) Uoyama, H.; Goushi, K.; Shizu, K.; Nomura, H.; Adachi, C. Highly Efficient Organic Light-Emitting Diodes from Delayed Flurescence. *Nature* **2012**, *492*, 234−238.
(7) Zhang, Q. S.; Li, B.; Huang, S. P.; Nomura, H.; Tanaka, H.; Adachi, C. Efficient Blue Organic Light-Emitting Diodes Employing Thermally Activated Delayed Flurescence. *Nat. Photonics* **2014**, *8*, 326−332.
(8) Li, W. J.; Pan, Y. Y.; Xiao, R.; Peng, Q. M.; Zhang, S. T.; Ma, D. G.; Li, F.; Shen, F. Z.; Wang, Y. H.; Yang, B.; Ma, Y. G. Employing ∼100% Excitons in OLEDs by Utilizing a Fluorescent Molecule with Hybridized Local and Charge-Transfer Excited State. *Adv. Funct. Mater.* **2014**, *24*, 1609−1614.
(9) Yao, L.; Zhang, S. T.; Wang, R.; Li, W. J.; Shen, F. Z.; Yang, B.; Ma, Y. G. Highly Efficient Near-Infrared Organic Light-Emitting Diode Based on a Butterfly-Shaped Donor−Acceptor Chromophore with Strong Solid-State Fluorescence and a Large Proportion of Radiative Excitons. *Angew. Chem.* **2014**, *126*, 2151−2155.
(10) Biczók, L.; Bérces, T.; Linschitz, H. Quenching Processes in Hydrogen-Bonded Pairs: Interactions of Excited Fluorenone with Alcohols and Phenols. *J. Am. Chem. Soc.* **1997**, *119*, 11071.
(11) Improta, R. Photophysics and Photochemistry of Thymine Deoxy-Dinucleotide in Water: A PCM/TD-DFT Quantum Mechanical Study. *J. Phys. Chem. B* **2012**, *116*, 14261.
(12) Klaumünzer, B.; Kröner, D.; Saalfrank, P. (TD-)DFT Calculation of Vibrational and Vibronic Spectra of Riboflavin in Solution. *J. Phys. Chem. B* **2010**, *114*, 10826.
(13) Ghosh, I.; Mukhopadhyay, A.; Koner, A. L.; Samanta, S.; Nau, W. M.; Moorthy, J. N. Excited-State Properties of Fluorenones: Influence of Substituents, Solvent and Macrocyclic Encapsulation. *Phys. Chem. Chem. Phys.* **2014**, *16*, 16436.
(14) Lin, S. H.; Chang, C. H.; Liang, K. K.; Chang, R.; Shiu, Y. J.; Zhang, J. M.; Yang, T. S.; Hayashi, M.; Hsu, F. C. Ultrafast Dynamics and Spectroscopy of Bacterial Photosynthetic Reaction Centers. *Adv. Chem. Phys.* **2002**, *121*, 1.
(15) Ianconescu, R.; Pollak, E. Photoinduced Cooling of Polyatomic Molecules in an Electronically Excited State in the Presence of Dushinskii Rotations. *J. Phys. Chem. A* **2004**, *108*, 7778.
(16) Niu, Y.; Peng, Q.; Shuai, Z. Promoting-Mode Free Formalism for Excited State Radiationless Decay Process with Duschinsky Rotation Effect. *Sci. China, Ser. B: Chem.* **2008**, *51*, 1153.
(17) Niu, Y. L.; Peng, Q.; Deng, C. M.; Gao, X.; Shuai, Z. G. Theory of Excited State Decays and Optical Spectra: Application to Polyatomic Molecules. *J. Phys. Chem. A* **2010**, *114*, 7817−7831.
(18) Peng, Q.; Niu, Y. L.; Shi, Q. H.; Gao, X.; Shuai, Z. G. Correlation Function Formalism for Triplet Excited State Decay: Combined Spin−Orbit and Nonadiabatic Couplings. *J. Chem. Theory Comput.* **2013**, *9*, 1132.
(19) Shi, Q. H.; Peng, Q.; Sun, S. R.; Shuai, Z. G. Vibration Correlation Function Investigation on the Phosphorescence Quantum Efficiency and Spectrum for Blue Phosphorescent Ir(III) Complex. *Acta Chim. Sin.* **2013**, *71*, 884−891.
(20) Tomasi, J.; Mennucci, B.; Cammi, R. Quantum Mechanical Continuum Solvation Models. *Chem. Rev.* **2005**, *105*, 2999.
(21) Improta, R. UV−Visible Absorption and Emission Energies in Condensed Phase by PCM-TD-DFT Methods. In *Computational Strategies for Spectroscopy: From Small Molecules to Nanosystems*; Barone, V., Ed.; John Wiley & Sons: Chichester, U.K., 2011; pp 39−76.
(22) Scalmani, G.; Frisch, M. J.; Mennucci, B.; Tomasi, J.; Cammi, R.; Barone, V. *J. Chem. Phys.* **2006**, *124*, 094107.
(23) Improta, R.; Barone, V.; Scalmani, G.; Frisch, M. J. *J. Chem. Phys.* **2006**, *125*, 54103.
(24) Improta, R.; Scalmani, G.; Frisch, M. J.; Barone, V. *J. Chem. Phys.* **2007**, *127*, 74504.
(25) Frisch, M. J.; Trucks, G. W.; Schlegel, H. B.; Scuseria, G. E.; Robb, M. A.; Cheeseman, J. R.; Scalmani, G.; Barone, V.; Mennucci, B.; Petersson, G. A.; et al. *Gaussian09*, revision D.01; Gaussian Inc.: Wallingford, CT, 2010.
(26) Peng, Q.; Yi, Y. P.; Shuai, Z. G.; Shao, J. S. Excited State Radiationless Decay Process with Duschinsky Rotation Effect: Formalism and Implementation. *J. Chem. Phys.* **2007**, *126*, 114302.
(27) Lin, S. H. Rate of Interconversion of Electronic and Vibrational Energy. *J. Chem. Phys.* **1966**, *44*, 3759−3767.
(28) Li, Z.; Suo, B.; Zhang, Y.; Xiao, Y.; Liu, W. Combining Spin-Adapted Open-Shell TDDFT with Spin−Orbit Coupling. *Mol. Phys.* **2013**, *111*, 3741.
(29) Li, Z.; Xiao, Y.; Liu, W. On the Spin Separation of Algebraic Two-Component Relativistic Hamiltonians. *J. Chem. Phys.* **2012**, *137*, 154114.
(30) Liu, W. Ideas of Relativistic Quantum Chemistry. *Mol. Phys.* **2010**, *108*, 1679.
(31) Liu, W.; Hong, G.; Dai, D.; Li, L.; Dolg, M. The Beijing Four-Component Density Functional Program Package (BDF) and Its Application to EuO, EuS, YbO and YbS. *Theor. Chem. Acc.* **1997**, *96*, 75.
(32) Chibani, S.; Le Guennic, B.; Charaf-Eddin, A.; Laurent, A. D.; Jacquemin, D. Revisiting the Optical Signatures of BODIPY with Ab Initio Tools. *Chem. Sci.* **2013**, *4*, 1950.
(33) Pedone, A. Role of Solvent on Charge Transfer in 7-Aminocoumarin Dyes: New Hints from TD-CAM-B3LYP and State Specific PCM Calculations. *J. Chem. Theory Comput.* **2013**, *9*, 4087.
(34) Improta, R. The Excited States of Π-Stacked 9-Methyladenine Oligomers: A TD-DFT Study in Aqueous Solution. *Phys. Chem. Chem. Phys.* **2008**, *10*, 2656.
(35) Jacquemin, D.; Mennucci, B.; Adamo, C. Excited-State Calculations with TD-DFT: From Benchmarks to Simulations in Complex Environments. *Phys. Chem. Chem. Phys.* **2011**, *13*, 16987.
(36) Chibani, S.; Charaf-Eddin, A.; Le Guennic, B.; Jacquemin, D. Boranil and Related NBO Dyes: Insights From Theory. *J. Chem. Theory Comput.* **2013**, *9*, 3127.
(37) Lu, T.; Chen, F. Multiwfn: A Multifunctional Wavefunction Analyzer. *J. Comput. Chem.* **2012**, *33*, 580.
(38) Lin, C.-K.; Li, M.-C.; Yamaki, M.; Hayashi, M.; Lin, S. H. A Theoretical Study on the Spectroscopy and the Radiative and Non-radiative Relaxation Rate Constants of the $S_0\ {}^1A_1 \rightarrow S_1\ {}^1A_2$ Vibronic Transitions of Formaldehyde. *Phys. Chem. Chem. Phys.* **2010**, *12*, 11432.
(39) Shuai, Z. G.; Peng, Q. Excited States Structure and Processes: Understanding Organic Light-Emitting Diodes at the Molecular Level. *Phys. Rep.* **2014**, *537*, 123−156.
(40) Shuai, Z. G.; Liu, W. J.; Liang, W. Z.; Shi, Q.; Chen, H. Theoretical Study of the Low-Lying Electronic Excited States for Molecular Aggregates. *Sci. China Chem.* **2013**, *56*, 1258−1262.
(41) *The Shuai Group Website*. http://www.shuaigroup.net/ (2014).